Available online at www.sciencedirect.com
SCIENCE DIRECT®
Surface Science 552 (2004) 98–110
SURFACE SCIENCE
www.elsevier.com/locate/susc

Ab initio DFT cluster studies of angle-resolved NEXAFS spectra for differently coordinated oxygen at the $V_2O_5(0\,1\,0)$ surface

C. Kolczewski, K. Hermann *

Theory Department, Fritz-Haber-Institut der Max-Planck-Gesellschaft, Faradayweg 4-6, D-14195 Berlin, Germany

Received 10 September 2003; accepted for publication 6 January 2004

Abstract

At the (0 1 0) surface of vanadium pentoxide, V_2O_5, there are differently coordinated oxygen centers (1-, 2-, 3-fold) which can participate as active sites in specific oxidation reactions. In the present work we use ab initio density functional theory together with cluster models to calculate 1s core excitation spectra of the differently coordinated oxygen centers at $V_2O_5(0\,1\,0)$. Corresponding excitation energies and dipole transition moments are determined by details of local V–O-binding where the results vary strongly with oxygen coordination. As a result, a strong dependence of the (angle-resolved) excitation spectra on oxygen coordination is found. The differences can also be seen in the superimposed spectrum combining excitations from all oxygen centers. A comparison of our theoretical spectra with experimental near edge X-ray absorption fine structure data yields good agreement and allows an assignment of the experimental peaks to the different surface oxygen centers.

Keywords: Density functional calculations; X-ray absorption spectroscopy; Clusters; Vanadium oxide; Oxygen; Near edge extended X-ray absorption fine structure (NEXAFS)

1. Introduction

Detailed knowledge of geometric and electronic properties of catalysts on a microscopic level is of great importance for an understanding of their reactivity in catalytic reactions and can help to design catalysts with better selectivity or reactivity [1–4]. Here we consider vanadium oxides which form a group of transition metal oxides that are widely used as active components in catalysts for many chemical reactions of industrial importance [5–7]. In these systems vanadium can appear in different oxidation states, from +2 to +5, as well as in different stoichiometry where four monovalent binary oxides are known, VO, VO_2, V_2O_3, and V_2O_5. Here we focus on V_2O_5 which is used, together with other elements such as bismuth, cobalt, aluminum, or alkali metals, as a selective catalyst component for redox or acid–base processes, such as the reduction of NO_x with NH_3 [8,9] or the selective oxidation of hydrocarbons [7,10,11].

At the surface of a vanadium oxide catalyst there are differently coordinated oxygen centers

* Corresponding author. Tel.: +49-30-84134812; fax: +49-30-84134701.
E-mail address: hermann@fhi-berlin.mpg.de (K. Hermann).

0039-6028/$ - see front matter © 2004 Elsevier B.V. All rights reserved.
doi:10.1016/j.susc.2004.01.013

which can participate in a catalytic reaction either as reactive sites or, in the case of oxidation reactions, become directly involved as reaction components. Here the different oxygen species are expected to react differently according to their specific binding environment [12,13]. Therefore, an analysis of the involvement of each species in particular reaction steps is essential for a detailed understanding of catalytic processes at the oxide surface. However, such analyses require an experimental identification of the differently coordinated oxygen species and its binding geometry which is rather difficult. The chemical differences between these species are quite subtle which can make a discrimination tedious and even impossible. For example, the 1s ionization potentials of the three differently coordinated (1- to 3-fold) oxygen species at the $V_2O_5(0\,1\,0)$ surface differ by only 0.5 eV as shown in recent theoretical studies [14]. This is consistent with X-ray photoemission spectroscopy (XPS) experiments on $V_2O_5(0\,1\,0)$ which exhibit only one broad peak in the energy region of O 1s ionization [15] that cannot be resolved further according to the different oxygen species.

An alternative spectroscopy that may enable an identification of differently coordinated oxygen in vanadium oxides may be near edge X-ray absorption fine structure (NEXAFS) spectroscopy. This spectroscopy is based on radiation induced excitations of core electrons to unoccupied states and has proven to be a powerful tool in studies of molecular structure as well as surface and adsorbate geometries [16–20]. Different atom species can be characterized by their K edge excitation energies and angle dependent measurements of absorption spectra yield information about the geometric arrangement of particular atoms in the system. However, the interpretation of the experimental spectra as to peak positions and intensities requires theoretical studies [21–25]. Recently, angle integrated NEXAFS spectra of the differently coordinated oxygen centers at the $V_2O_5(0\,1\,0)$ surface have been evaluated in ab initio density functional theory (DFT) cluster studies [14]. The theoretical spectra show a clear distinction between the different oxygen centers where spectral details can be explained by binding properties of the final state orbitals depending on the environmental geometry and coordination. The distinction is expected to become even more obvious in angle-resolved NEXAFS spectra where transition matrix elements, determining corresponding absorption intensities, can be easily connected with the directionality of inter-atomic binding and that of the polarization vector of the exciting photon beam. In addition, angle-resolved theoretical spectra for O 1s core excitation at the $V_2O_5(0\,1\,0)$ surface can be directly compared with corresponding NEXAFS measurements which have become available recently [26].

In the present work we have extended our theoretical treatment to evaluate angle-resolved NEXAFS spectra in order to study the behavior of differently coordinated oxygen at the $V_2O_5(0\,1\,0)$ surface using O 1s core excitation. Section 2 introduces our methods and discusses technical details. Section 3 presents our results and compares with recent NEXAFS experiments [26] while Section 4 summarizes our conclusions.

2. Computational details

Bulk vanadium pentoxide, V_2O_5, crystallizes in a layer type orthorhombic structure with lattice constants $a = 11.519$ Å, $b = 4.373$ Å, $c = 3.564$ Å where the elementary cell contains 14 atoms ($= 2\times V_2O_5$) [27], see Fig. 1. The crystal layers extend parallel to (0 1 0) netplanes and can be characterized by periodic networks of VO_5 pyramids sticking out at both sides of the layer. There are three differently coordinated oxygen centers in the layers: terminal (vanadyl) oxygen, O(1), coordinated to one vanadium center through a short bond ($d_{V\text{–}O} = 1.58$ Å) and bridging oxygen, O(2)/O(3), coordinated to two or three vanadium centers with V–O distances ranging between 1.78 and 2.01 Å. This gives rise to five structurally different surface oxygen centers, singly coordinated O(1), doubly coordinated O(2) and O(2′), and triply coordinated O(3) and O(3′), as shown in Fig. 1.

In the simulation of local sections of the crystal layers we use the $V_{10}O_{31}H_{12}$ cluster shown in Fig. 2. This cluster contains the three different oxygen species, O(1–3), in a realistic environment of its

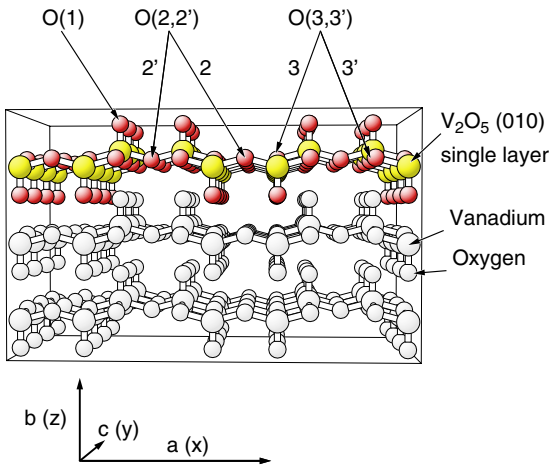

Fig. 1. Crystal structure of orthorhombic V_2O_5 for a view along the (0 0 1) direction (perpendicular to (0 1 0)) where the topmost (0 1 0) single layer is emphasized by shading. Vanadium centers are shown by large light balls and oxygen centers by smaller dark balls. The non-equivalent oxygen centers, O(1–3, 2′, 3′) of the crystal are labeled accordingly. The figure includes a sketch of the orthorhombic lattice vectors at the bottom. (For a colour version, see the online paper.)

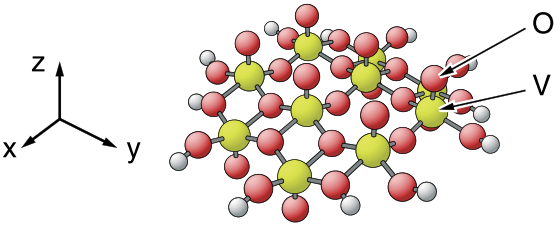

Fig. 2. Geometric structure of the $V_{10}O_{31}H_{12}$ cluster representing a local section of the V_2O_5(0 1 0) crystal layer. Vanadium centers are shown by large light balls and oxygen centers by smaller dark balls while the smallest light balls refer to hydrogen saturator atoms at the cluster periphery. (For a colour version, see the online paper.)

nearest neighbors inside the V_2O_5(0 1 0) layer. In addition, cluster embedding in the layer is achieved by saturating dangling bonds at the cluster periphery by hydrogen. The $V_{10}O_{31}H_{12}$ cluster has proven to yield a reliable description of electronic properties of (0 1 0) oriented V_2O_5 crystal layers and surfaces [27,28] and has been used in previous calculations on angle integrated NEXAFS spectra [14].

The electronic structure of the cluster is evaluated by DFT methods using gradient-corrected exchange and correlation functionals according to Perdew et al. [29,30]. Corresponding Kohn–Sham cluster orbitals are described by local basis sets of linear combinations (LCAO's) of contracted Gaussians and calculated with the cluster code StoBe [31]. This code allows, in addition to ground state calculations, the evaluation of NEXAFS spectra based on the transition state approach [32,33] in combination with a double basis set technique [34]. Here relaxed molecular orbitals of the core hole excited final states are determined using good quality basis sets, see below, with a half-occupied core orbital at the ionization site. Improved orbitals of the excited electrons are then obtained by diagonalizing the Kohn–Sham matrix built from the initial density with an additional diffuse basis set (about 150–300 functions) centered at the excited atom. The resulting orbital energies and dipole transition matrix elements (oscillator strengths) are found to provide a good representation of the excitations yielding the theoretical NEXAFS spectrum. For a detailed description of the present method see [35].

The Gaussian basis sets used in this study consist of double zeta valence plus polarization (DZVP) bases in a [5s,3p,2d] contraction for vanadium and a [4s,1p] basis set for hydrogen [36]. For oxygen different basis sets are used. In the calculations of O 1s core excitation the oxygen at the ionization site is described by an IGLO-III basis [37] in order to obtain a reliable description of inner shell relaxation effects. The other oxygen centers in the cluster are described by an effective core potential (ECP) [38] together with a [5s4p1d] valence basis to avoid explicit mixing of 1s orbitals of different oxygen centers with that of the ionization site. This approximation has proven to introduce only negligible errors in the computed excitation spectrum [39]. In order to improve the representation of orbitals near ionization threshold in the last step of the spectral calculation a large diffuse [19s19p19d] basis set is added at the excitation site. The discrete set of computed excitations is then used to evaluate a continuous NEXAFS spectrum by Gaussian convolution with varying energy broadening. In the energy region

below ionization threshold a constant broadening (FWHM) of 1.0 eV is applied while for higher energies (up to 10 eV above ionization) the broadening is increased linearly to 4.5 eV and kept constant at 4.5 eV at even higher energies. The relatively large broadening of 4.5 eV at higher energies is necessary in order to correct for the approximate description of the continuum wavefunctions by diffuse localized basis functions. It should be noted that the present use of localized basis sets to represent propagating continuum wavefunctions (which describe NEXAFS final states) cannot be exact. However, the approximation is found to be quite satisfactory within the highly localized region of the core orbitals which participate in the NEXAFS transitions. As a result, corresponding dipole transition matrix elements, determining spectral NEXAFS intensities, are believed to be rather reliable.

The calculation of NEXAFS spectra in the present work is based on core to excited orbital excitations which are determined by dipole transitions. Hence, angle-resolved spectral intensities are given by corresponding dipole transition matrix elements, m_x, m_y, m_z, involving the initial core orbital φ_i and final excited state orbitals φ_f with

$$\underline{m} = (m_x, m_y, m_z) = \langle \varphi_f | q \cdot \underline{r} | \varphi_i \rangle \tag{1}$$

(q denoting the electron charge) together with angular dependent factors describing the polarization vector of the incoming radiation

$$\begin{aligned} \underline{e} &= (e_x, e_y, e_z) \\ &= (\sin\vartheta\cos\varphi, \sin\vartheta\sin\varphi, \cos\vartheta) \end{aligned} \tag{2}$$

according to

$$\begin{aligned} I(E,\vartheta,\varphi) &= \alpha \cdot E \cdot (\underline{m}\,\underline{e})^2 \\ &= \alpha \cdot E \cdot (m_x e_x + m_y e_y + m_z e_z)^2 \\ &= \alpha \cdot E \cdot \{\sin^2\vartheta (m_x\cos\varphi + m_y \sin\varphi)^2 \\ &\quad + \cos^2\vartheta m_z^2 \\ &\quad + 2\sin\vartheta\cos\vartheta (m_x\cos\varphi + m_y\sin\varphi) m_z\} \end{aligned} \tag{3}$$

while the angle integrated intensity is given by

$$\begin{aligned} I(E) &= \int I(E,\vartheta,\varphi)\,\mathrm{d}\Omega \\ &= 4\pi/3 \cdot \alpha \cdot E \cdot (m_x^2 + m_y^2 + m_z^2) \end{aligned} \tag{4}$$

where E denotes the transition energy and α is a global scaling factor.

Ideally, initial core and final state orbitals, φ_i and φ_f, determining transition matrix elements (1) have to be evaluated for each transition separately, taking orbital relaxation due to the presence of the core hole and the excited electron into account. For large systems and many excited states this procedure is very tedious. Therefore, we use an approximate treatment for the present system which has proven to be quite successful for molecular NEXAFS spectra [16–19,21]. Here we assume that electronic relaxation is quite important for the highly localized core orbital φ_i. Thus, the orbital is taken from a calculation on the corresponding core hole state treated in Slater's transition state approach [32,33] (using occupation $\frac{1}{2}$ for the respective core orbital). Further, electronic relaxation of the final state orbitals φ_f is believed to be rather small since these orbitals are generally quite diffuse. Therefore, we neglect this relaxation and use final state orbitals φ_f of the same core hole state calculation described before. As a result, the evaluation of the complete excitation spectrum can be based on only one self-consistent calculation. The approximate treatment of electronic relaxation in the core hole excited state yields excitation and ionization energies which are too large by 1.5–2 eV [40], compared with experiment. This difference can be rationalized for the present system by comparing the corresponding core ionization potential $\mathrm{IP}_{\mathrm{relaxed}}$ obtained for the fully relaxed core hole state with that, $\mathrm{IP}_{\mathrm{ts}}$, of Slater's transition state approach described above. This yields a value of 1.8 eV, see Table 1, which we apply as a global relaxation shift for all excitation energies in direct comparisons with experiment, Fig. 8, assuming that relaxation corrections vary only slightly with energy. (Note that except for Fig. 3 (taken from previous work [14]) all purely theoretical spectra, Figs. 4–7 and 9, do not include the global relaxation shift.) Further corrections, such as due to relativistic effects, are not included in the present calculations.

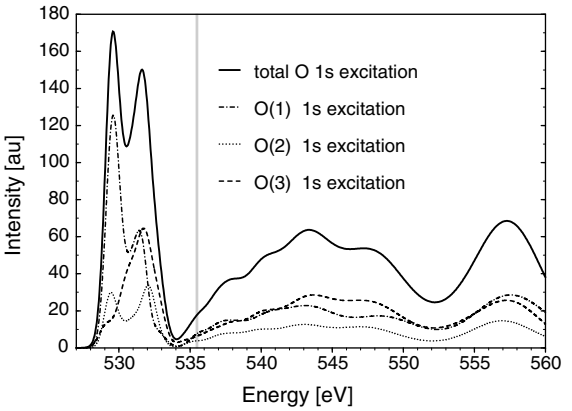

Fig. 3. O 1s core level excitation spectrum for the $V_{10}O_{31}H_{12}$ cluster, see text. The total spectrum is decomposed into contributions due to the differently coordinated oxygen, O(1), O(2), and O(3), shown by dotted, dashed, and dash-dotted lines, respectively. The gray vertical line near 535 eV indicates the ionization limit. The spectrum is shifted by 1.8 eV to correct for the relaxed values of the O 1s ionization potentials, see Section 2 and Table 1.

Table 1
O 1s core ionization potentials (IP) of differently coordinated oxygen O(1, 2, 3) at the $V_2O_5(0\,1\,0)$ surface using a $V_{10}O_{31}H_{12}$ cluster model. The table compares values of frozen orbital IP's (IP_{frozen}) with those of the transition state approach (IP_{ts}) and of the fully relaxed core ion state ($IP_{relaxed}$), see text. All energies are in eV

	IP_{frozen}	IP_{ts}	$IP_{relaxed}$
O(1)	566.95	537.48	535.63
O(2)	566.59	537.20	535.43
O(3)	566.47	537.30	535.52

The present approach used to evaluate NEXAFS spectra differs substantially from that used in a previous study on V K-edge spectra of V_2O_5 [25]. The latter is based on real-space multiple-scattering calculations in a non-self-consistent muffin-tin potential where specific core excitations are included only approximately by corresponding phase shifts.

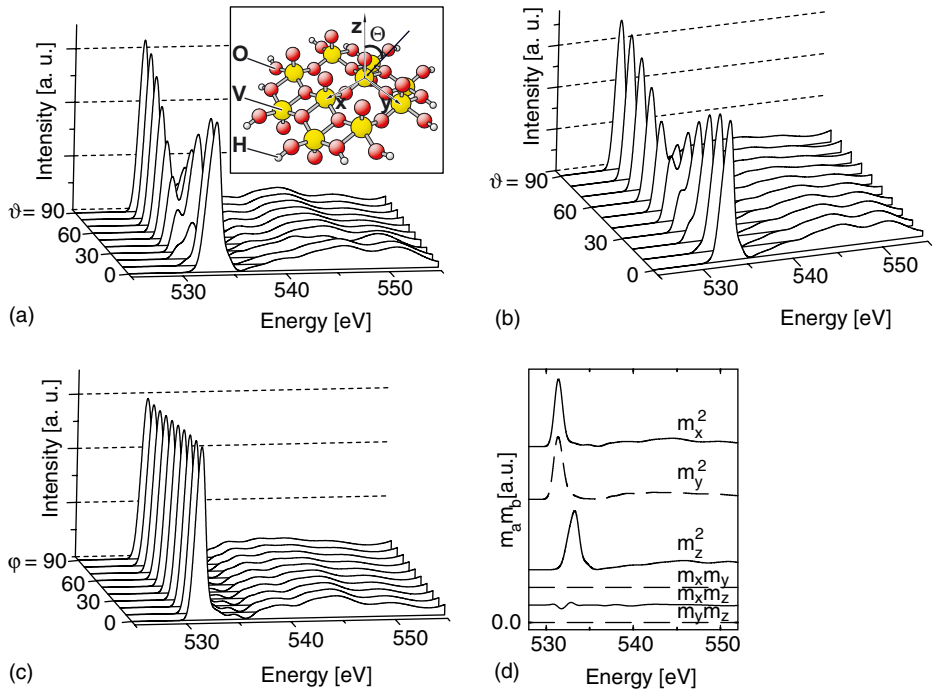

Fig. 4. Angle-resolved O 1s NEXAFS spectra for terminal oxygen O(1) simulating X-ray polarization along (a) the *xz* plane ($\vartheta = 0$–$90°$), $\varphi = 0°$), (b) the *yz* plane ($\vartheta = 0$–$90°$), $\varphi = 90°$), and (c) the *xy* plane ($\vartheta = 90°$, $\varphi = 0$–$90°$). The plane and angle definitions are given in the inset of Fig. 4(a). Fig. 4(d) shows the energy dependence of the dipole transition terms m_x^2, m_y^2, m_z^2, $m_x m_y$, $m_x m_z$, and $m_y m_z$, see text.

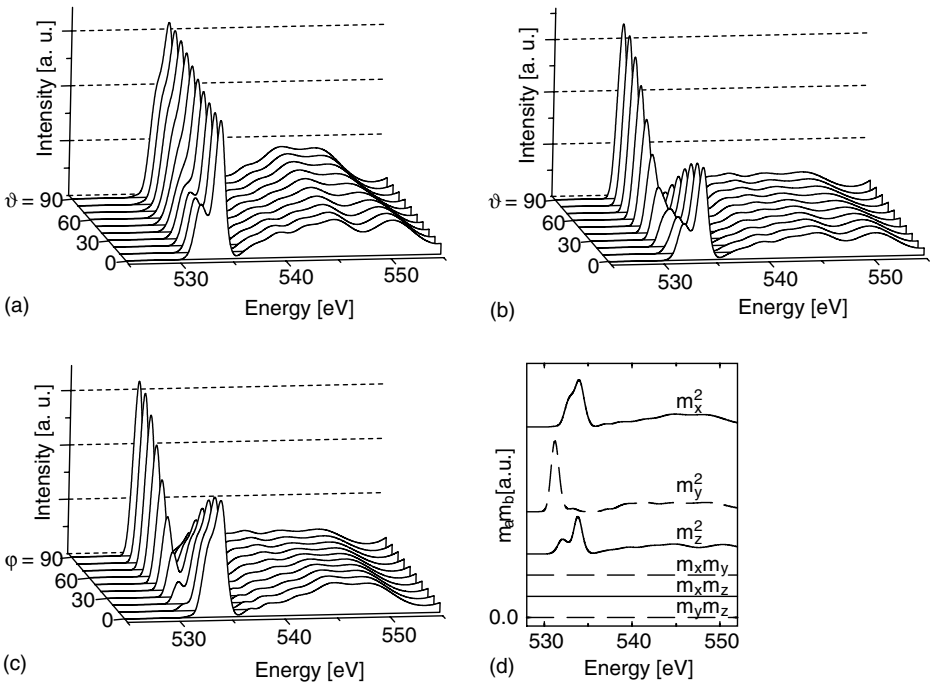

Fig. 5. Angle-resolved O 1s NEXAFS spectra for 2-fold bridging oxygen O(2) simulating X-ray polarization along (a) the *xz* plane ($\vartheta = 0$–$90°$, $\varphi = 0°$), (b) the *yz* plane ($\vartheta = 0$–$90°$, $\varphi = 90°$), and (c) the *xy* plane ($\vartheta = 90°$, $\varphi = 0$–$90°$). The plane and angle definitions are given in the inset of Fig. 4(a). Fig. 5(d) shows the energy dependence of the dipole transition terms m_x^2, m_y^2, m_z^2, m_xm_y, m_xm_z, and m_ym_z, see text.

3. Results and discussion

In Fig. 3 we summarize results from previous calculations [14] of angle integrated NEXAFS spectra for differently coordinated oxygen centers in V_2O_5. The stoichiometric superposition of the atom resolved spectra shows a double-peak structure below ionization threshold, in the region 530–532 eV, which has been explained by analyses of the final state orbitals [14]. The lower energy peak is determined mainly by excitation of the singly coordinated vanadyl oxygen, O(1), while the higher peak contains contributions from all three different oxygen centers. The computed 1s ionization potentials of the different oxygen species in V_2O_5, indicated by a vertical gray line in Fig. 3, differ by less than 0.3 eV. This explains why photoionization cannot discriminate between the different oxygen species. Fig. 3 shows in the energy region above ionization threshold a broad resonance between 540 and 550 eV which is assigned to transitions into O 3p type final states. A decomposition of the total spectrum into atom resolved contributions due to differently coordinated oxygen reveals substantial differences, in particular, within the energy region of the double-peak structure. It may, therefore, be used to discriminate between the oxygen species. However, a decomposition of the angle integrated NEXAFS spectrum cannot be directly used to compare with NEXAFS experiments for the $V_2O_5(0\,1\,0)$ surface which yield always angle-resolved spectra for given X-ray beam polarization with respect to the surface normal. Thus, we have computed angle-resolved spectra for the differently coordinated oxygen species at the $V_2O_5(0\,1\,0)$ surface according to Eq. (3).

Fig. 4(a) shows theoretical angle-resolved NEXAFS spectra for core excitation of singly coordinated oxygen O(1) at the $V_2O_5(0\,1\,0)$ surface with the X-ray beam polarized in the *xz* plane, see

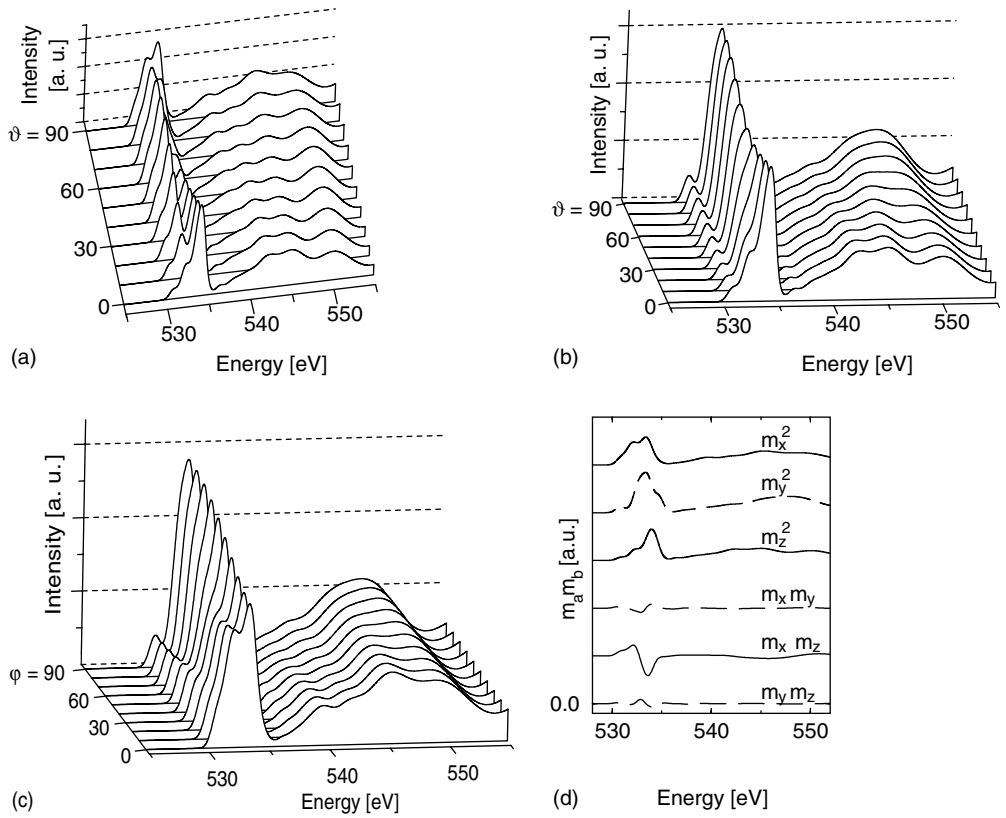

Fig. 6. Angle-resolved O 1s NEXAFS spectra for 3-fold bridging oxygen O(3) simulating X-ray polarization along (a) the xz plane ($\vartheta = 0$–$90°$, $\varphi = 0°$), (b) the yz plane ($\vartheta = 0$–$90°$, $\varphi = 90°$), and (c) the xy plane ($\vartheta = 90°$, $\varphi = 0$–$90°$). The plane and angle definitions are given in the inset of Fig. 4(a). Fig. 6(d) shows the energy dependence of the dipole transition terms m_x^2, m_y^2, m_z^2, $m_x m_y$, $m_x m_z$, and $m_y m_z$, see text.

inset of Fig. 4(a), where the polar angle ϑ of the polarization vector $\underline{e}$ with respect to the surface normal varies between 0° and 90° (with fixed azimuthal $\varphi = 0°$). For this geometry Eq. (3) yields an angular variation of the absorption

$$I(E, \vartheta, \varphi = 0°) = \alpha \cdot E \cdot \{\sin^2 \vartheta m_x^2 + \cos^2 \vartheta m_z^2 + \sin 2\vartheta m_x m_z\} \quad (5)$$

involving only dipole transition matrix elements m_x, m_z. Fig. 4(b) shows analogous spectra for the X-ray beam polarized in the yz plane (fixed azimuthal angle $\varphi = 90°$). Here Eq. (3) yields for the absorption

$$I(E, \vartheta, \varphi = 90°) = \alpha \cdot E \cdot \{\sin^2 \vartheta m_y^2 + \cos^2 \vartheta m_z^2 + \sin 2\vartheta m_y m_z\}. \quad (6)$$

Fig. 4(c) displays spectra for the X-ray beam polarized in the xy plane (normal incidence, fixed polar angle $\vartheta = 90°$) where Eq. (3) yields for the absorption

$$I(E, \vartheta = 90°, \varphi) = \alpha \cdot E \cdot \{\cos^2 \varphi m_x^2 + \sin^2 \varphi m_y^2 + \sin 2\varphi m_x m_y\}. \quad (7)$$

Fig. 4(a,b) reveal that the above equations lead to a strong angular dependence of the absorption for both geometries. It is explained by the involvement of the energy dependent dipole transition matrix elements m_x, m_y, m_z determined by the character of corresponding final state orbitals. This becomes evident in Fig. 4(d) where the energy dependent contributions $m_a m_b, a, b = x, y, z$, appearing in Eqs. (5)–(7) are displayed. (The different

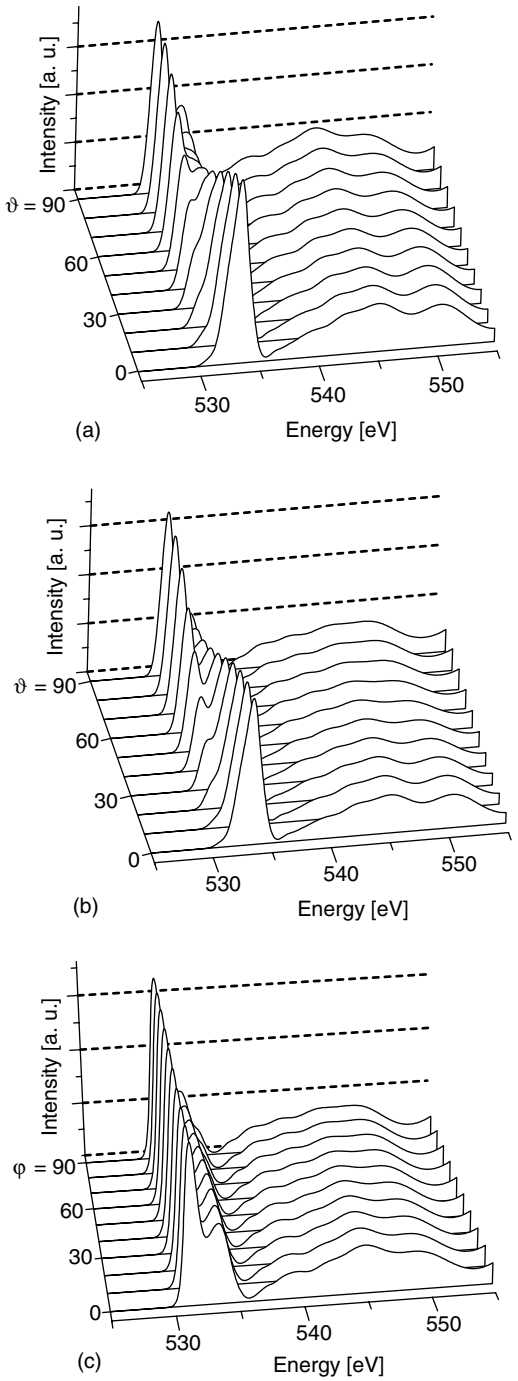

Fig. 7. Angle-resolved O 1s NEXAFS spectra for the stoichiometric atom superposition of the $V_2O_5(0\,1\,0)$ surface, see text. The X-ray beam is polarized along (a) the *xz* plane ($\vartheta = 0$–$90°$, $\varphi = 0°$), (b) the *yz* plane ($\vartheta = 0$–$90°$, $\varphi = 90°$), and (c) the *xy* plane ($\vartheta = 90°$, $\varphi = 0$–$90°$). The plane and angle definitions are given in the inset of Fig. 4(a).

curves of Fig. 4(d) are obtained by smoothing discrete distributions of transitions and are shifted vertically with respect to each other in order to improve their discrimination. All curves meet the left figure frame with a $m_a m_b$ value equal to zero.) Obviously, for O(1) 1s excitation the mixed contributions $m_x m_y$, $m_x m_z$, $m_y m_z$ are found to be negligible in size compared with the m_x^2, m_y^2, m_z^2 contributions (<0.01% for $m_x m_y$, $m_y m_z$, <10% for $m_x m_z$) and can be ignored in the following discussion. Dipole contributions m_x^2 (m_y^2) are largest in the energy range of 531–532 eV where transitions to final state orbitals with anti-bonding O $2p_x$ ($2p_y$) and V $3d_{xz}$ ($3d_{yz}$) mixtures occur. In contrast, contributions m_z^2 are largest for energies about 533 eV referring to final state orbitals described by anti-bonding O $2p_z$ and V $3d_z^2$ mixtures. As a result, the angle dependent NEXAFS spectra, both $I(E, \vartheta, \varphi = 0°)$ and $I(E, \vartheta, \varphi = 90°)$, are described in the energy range between 530 and 535 eV by double-peak structures with ϑ dependent relative peak heights. For small ϑ values the peak at larger energy (about 533 eV) dominates while for ϑ close to 90° the low-energy peak (about 531 eV) becomes more important, see Figs. 4(a,b). Further, the similarity between the energy dependence of m_x^2 and m_y^2 explains that the absorption for normal X-ray incidence, $I(E, \vartheta = 90°, \varphi)$, is almost independent of the azimuthal angle φ, see Fig. 4(c).

Fig. 5(a)–(c) show the theoretical angle-resolved NEXAFS spectra for core excitation of doubly coordinated oxygen O(2) at the $V_2O_5(0\,1\,0)$ surface. The angular dependence of the spectra is very pronounced in all three cases, polarization in the *xz* plane, Fig. 5(a), in the *yz* plane, Fig. 5(b), and in the *xy* plane, Fig. 5(c) and different from that found for O(1) excitation. This originates from differences in the energy dependence of the dipole transition matrix elements shown in Fig. 5(d). As before, the mixed contributions $m_a m_b$, $a \neq b$ can be neglected in the intensities, Eqs. (5)–(7), due to their size while the square terms m_a^2 yield an energy dependence different to that for O(1) 1s excitation. The m_x^2 contribution is largest for energies between 533 and 535 eV where transitions into final state orbitals described as anti-bonding mixtures of O $2p_x$ and V $3d_{x^2-y^2}$ occur. The O(2) $2p_x$ orbital is pointing directly towards

the nearest neighbor vanadium centers and builds rather strongly anti-bonding combinations with vanadium orbitals which explains the high transition energy, see [14] for a detailed discussion. In contrast, m_y^2 is largest at lower transition energies, 531–532 eV, corresponding to transitions into final state orbitals characterized as weaker anti-bonding O $2p_y$–V $3d_{xy}$ combinations. Further, the energy dependence of m_z^2 reveals a two-peak structure, see Fig. 5(d), with a low-energy peak at 532 eV, corresponding to excitations into anti-bonding O $2p_z$–V $3d_{xz}$ orbitals. The peak at 534 eV is due to transitions into orbitals containing O $2p_z$ and V $3d_z^2$ character where the vanadium contributions are strongly anti-bonding with respect to $2p_z$ orbitals of adjacent vanadyl oxygen. As a result, the theoretical NEXAFS spectrum $I(E,\vartheta,\varphi=0°)$, Eq. (5) and Fig. 5(a), exhibits a double-peak structure between 530 and 535 eV with the high-energy peak being always the largest. In contrast, the spectrum $I(E,\vartheta,\varphi=90°)$, Eq. (6) and Fig. 5(b), yields a double-peak structure where the high-energy peak dominates at small angles ϑ while the low-energy peak becomes important for angles ϑ close to 90°. Further, the different energy dependence of the m_x^2 and m_y^2 contributions explains the angular dependence of the X-ray spectra for normal incidence, $I(E,\vartheta=90°,\varphi)$, Eq. (7) and Fig. 5(c).

Fig. 6(a)–(c) show the theoretical angle-resolved NEXAFS spectra for core excitation of 3-fold coordinated oxygen O(3) at the V_2O_5(0 1 0) surface where the X-ray polarization directions are chosen identical to those for O(1) and O(2) excitation, Figs. 4(a)–(c), 5(a)–(c). As before, the spectra can be explained by the energetic behavior of the matrix element products $m_a m_b$, see Fig. 6(d), which differs substantially from that for both O(1) and O(2) excitation, see Figs. 4(d) and 5(d). For O(3) excitation, the three square terms m_x^2, m_y^2, m_z^2 yield broad distributions of rather similar shape in the energy range between 532 and 535 eV. In addition, the mixed term $m_x m_z$ becomes comparable in size with the square terms where both additive and subtractive contributions are found, Fig. 6(d). The latter is explained by the complex binding situation at the O(3) site which involves O $2p_x$, $2p_y$, and $2p_z$ orbitals as discussed in [14]. Therefore, the angle dependent NEXAFS spectra, $I(E,\vartheta,\varphi=0°)$ of Fig. 6(a) show two-peak structures between 530 and 535 eV where the low-energy peak increases in size with increasing ϑ reaching a maximum near 60° due to the additive contribution $\sin 2\vartheta m_x m_z$, see Eq. (5). Likewise, the high-energy peak assumes a minimum at $\vartheta = 45°$. The spectra $I(E,\vartheta,\varphi=90°)$ and $I(E,\vartheta=90°,\varphi)$, shown in Fig. 6(b,c), can also be explained by the energy dependent square terms m_a^2 together with the angle variations as discussed before.

A stoichiometric superposition of the angle-resolved NEXAFS spectra from the individual oxygen centers yields total spectra that can be compared with experiment. The spectra for polar angle variations, $I(E,\vartheta,\varphi=0°)$ and $I(E,\vartheta,\varphi=90°)$, see Fig. 7(a,b), show a clear angle dependence which is qualitatively similar and consistent with experimental results by Goering et al. [41]. In both cases there is a two-peak structure between 530 and 535 eV where for small angles ϑ the high-energy peak dominates. This peak is determined by transitions to final state orbitals described as strongly anti-bonding combinations of O(1–3) $2p_z$ orbitals with corresponding V 3d orbitals. For larger ϑ values the low-energy peak gains intensity at the expense of that at higher energy. Here the low-energy peak for *xz* polarization, referring to $I(E,\vartheta,\varphi=0°)$, originates from transitions to final state orbitals characterized by more weakly anti-bonding combinations of O(1) $2p_x$ with corresponding V 3d orbitals. For *yz* polarization, $I(E,\vartheta,\varphi=90°)$, this peak belongs to final state orbitals described as anti-bonding combinations of O(1) $2p_y$ and O(2) $2p_y$ with V 3d. The spectra for normal X-ray incidence and azimuthal angle variation, $I(E,\vartheta=90°,\varphi)$, see Fig. 7(c), exhibit a two-peak structure where the peaks depend very little on the angle φ. This result is consistent with recent NEXAFS experiments [26] and is caused by the fact that the corresponding O(1) 1s excitation spectra, Fig. 4(c), show no dependence on φ while the angle dependences of the O(2) and O(3) excitation spectra, Figs. 5(c) and 6(c), counterbalance each other.

A comparison of the present theoretical results with recent experimental NEXAFS data [26] for V_2O_5(0 1 0) is shown in Fig. 8 where the

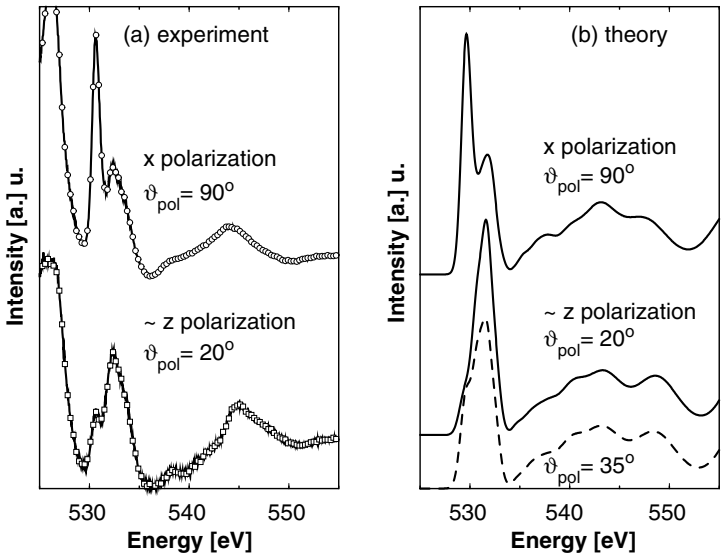

Fig. 8. Comparison of (a) experimental spectra from NEXAFS studies [26] of the V_2O_5(0 1 0) surface with (b) the theoretical total O 1s core level excitation spectrum. The spectra refer to *xz* polarization and two different polar angles ϑ_{pol}. The dashed curve in Fig. 8(b) shows the theoretical spectrum for $\vartheta_{pol} = 35°$, see text. All theoretical spectra are shifted rigidly by 1.8 eV to reflect the relaxed ionization potential, see Section 2 and Table 1.

measurements refer to two different X-ray polarization directions only, *x* polarization ($\vartheta = 90°$, $\varphi = 0°$, normal incidence of the X-ray beam), and near *z* polarization ($\vartheta = 20°$, $\varphi = 0°$, near grazing incidence). For *x* polarization the agreement between theory and experiment is almost perfect. Both the energetic positions and the intensities of the two peaks in the energy range between 530 and 535 eV are reproduced by the calculated spectrum. In addition, the broad peak in the continuum region near 545 eV, assigned to transitions into O 3p orbitals, is well reproduced. For X-ray polarization near the *z* direction the agreement between theory and experiment is somewhat less satisfactory. The energetic position of the peak at 532 eV is reproduced in the theoretical spectrum and a small shoulder at lower energy becomes visible. The latter may correspond to the small low-energy peak in the experiment but the intensity ratio of the two peaks does not agree well. This may be due to corrections in the experimental polar angle ϑ. In fact, Fresnel diffraction effects could modify the effective angle of incidence and thus ϑ compared with the initial value determined by beam adjustment. As an illustration, Fig. 8 includes a theoretical spectrum for $\vartheta = 35°$, $\varphi = 0°$ (dashed line) which yields better agreement with the experiment for $\vartheta = 20°$ assumed from beam adjustment. The experimental spectra include excitation peaks at energies lower than 530 eV which are caused by excitations of V 2p core electrons to V 3d final state orbitals and which are not accounted for by the present theory.

An analysis of the angle-resolved NEXAFS spectra for O 1s excitation, in particular those for normal X-ray incidence, $I(E, \vartheta = 90°, \varphi)$, in the energy range between 530 and 535 eV allows a discrimination of the differently coordinated oxygen centers in V_2O_5 based on peak intensities. The theoretical spectra for *x* polarization, $I(E, \vartheta = 90°, \varphi = 0°)$, see Fig. 9(a) (collecting spectra from Figs. 4(a), 5(a) and 6(a)), are determined by matrix elements m_x according to Eq. (5). Thus, transitions to final state orbitals containing admixtures of O $2p_x$ orbitals become most important. For O(1) excitation these transitions belong to the low-energy peak of the spectrum whereas for O(2) and O(3) excitations they refer to the high-energy peak. Therefore, the low-energy peak in the combined spectrum for *x* polarization, $I(E, \vartheta = 90°, \varphi = 0°)$

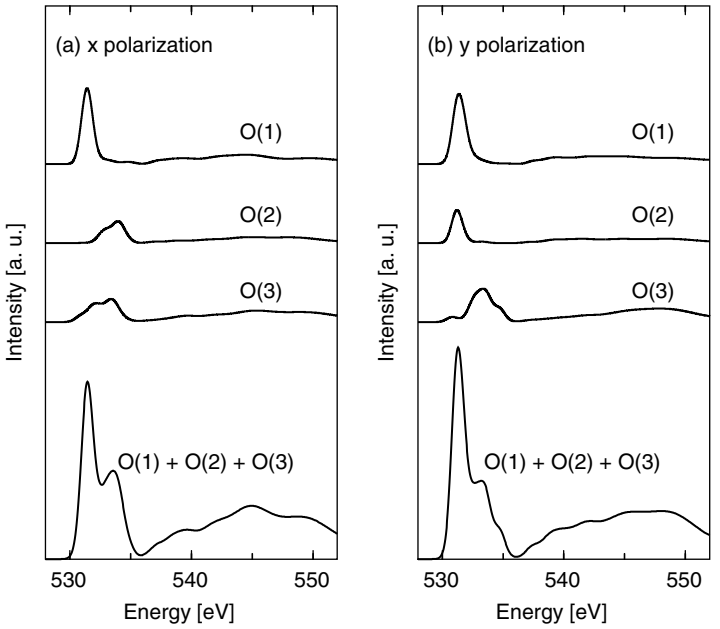

Fig. 9. Theoretical O 1s NEXAFS spectra of V_2O_5(0 1 0) for O(1) oxygen (dashed line), for O(2) (dotted line), for O(3) (dashed-dotted line), and for the stoichiometric atom superposition (2×O(1) + O(2) + 2×O(3), solid line). The X-ray beam is polarized along (a) the x direction ($\vartheta = 90°$, $\varphi = 0°$), and (b) the y direction ($\vartheta = 90°$, $\varphi = 90°$. Angle definitions are given in the inset of Fig. 4(a). The curves are taken from Figs. 4(a,b), 5(a,b), 6(a,b) and 7(a,b).

of Fig. 9(a), can be clearly assigned to the singly coordinated vanadyl oxygen center O(1). On the other hand, the spectra for y polarization, $I(E, \vartheta = 90°, \varphi = 90°)$, see Fig. 9(b) (collecting spectra from Figs. 4(b), 5(b) and 6(b)), are determined by matrix elements m_y according to Eq. (6). Thus, transitions to final state orbitals containing admixtures of O $2p_y$ orbitals dominate the spectrum. For O(1) and O(2) excitations these transitions belong to the low-energy peak of the spectrum whereas for O(3) excitation they refer to the high-energy peak. Therefore, the high-energy peak in the combined spectrum for y polarization, $I(E, \vartheta = 90°, \varphi = 90°)$ of Fig. 9(b), refers mainly to the 3-fold coordinated oxygen center O(3). The present theoretical NEXAFS spectra do not allow an unambiguous assignment of the doubly coordinated bridging oxygen center O(2) to an absorption peak for a given X-ray polarization. Whenever one of the two peaks in the energy range between 530 and 535 eV contains large contributions due to excitations at O(2) there are also contributions from O(1) and/or O(3) excitations.

The identification of differently coordinated oxygen centers in V_2O_5 by angle-resolved NEXAFS spectra can become useful in adsorption or catalytic reaction studies at the oxide surface. Here the question arises as to which of the differently coordinated surface oxygen centers acts as an adsorption site or is involved in a particular surface reaction. This may be answered by comparing angle-resolved NEXAFS spectra for normal X-ray incidence $I(E, \vartheta = 90°, \varphi)$ in the energy range of O 1s excitation where the spectra for the system concerned are obtained before and after the adsorption/reaction has taken place. The adsorption/reaction is assumed to influence the spectra depending on the oxygen coordination. Therefore, details of the spectral changes may give information about the type of oxygen center which is involved. Considering the above discussion we can suggest two rules. (a) If in measurements of $I(E, \vartheta = 90°, \varphi = 0°)$ the low-energy peak of the two-peak structure between 530 and 535 eV is mainly affected, the singly coordinated vanadyl center O(1) is involved in the adsorption/reaction.

(b) If in measurements of $I(E, \vartheta = 90°, \varphi = 90°)$ the high-energy peak of the two-peak structure between 530 and 535 eV is mainly affected, the 3-fold coordinated center O(3) is involved in the adsorption/reaction.

4. Conclusions

In this work we present theoretical angle-resolved NEXAFS spectra for O 1s excitation of the differently coordinated oxygen centers at the $V_2O_5(0\,1\,0)$ surface and in its bulk volume using ab initio DFT cluster methods. The results allow a very detailed analysis of the different excitation peaks and their angular variation based on the character of corresponding final state orbitals and the energy dependence of respective dipole transition matrix elements. In particular, the two-peak structure found in the energy range between 530 and 535 eV is characterized by excitations from O 1s core to final state orbitals which are antibonding mixtures of O 2p and V 3d contributions. The peak intensities for a given excitation energy and X-ray polarization depend on details of the orbital mixing in the final states, in particular, on the relative importance of orbital $2p_x$, $2p_y$, and $2p_z$ contributions at the oxygen center where the core electron is excited. Clearly, these orbital contributions are determined by the binding environment and coordination of the corresponding oxygen species. This allows an unambiguous assignment of the two excitation peaks to specific oxygen centers if the X-ray polarization in the NEXAFS spectrum is chosen appropriately. In particular, the analysis of the theoretical spectra for normal X-ray incidence in the $V_2O_5(0\,1\,0)$ system shows that

(a) with x polarization the low-energy peak of the two-peak structure between 530 and 535 eV is dominated by contributions referring to the singly coordinated vanadyl center O(1),
(b) with y polarization the high-energy peak of the two-peak structure contains mainly contributions referring to the 3-fold coordinated center O(3).

This can be made use of in adsorption or catalytic reaction studies at the oxide surface where the differently coordinated surface oxygen species has to be analyzed with respect to its participation as an adsorption site or its involvement in a particular surface reaction. A comparison of angle-resolved NEXAFS spectra for normal X-ray incidence taken before and after the adsorption/reaction yields differences in peak intensities which can help to identify the oxygen species where the action happens if the above two rules are applied.

The agreement between the present theoretical spectra and those of recent NEXAFS measurements for $V_2O_5(0\,1\,0)$ for two different X-ray polarization directions [26] is very satisfactory and confirms that an interpretation of experimental spectra by the present theoretical methods is adequate. A more detailed comparison between theory and experiment will be possible when measurements of a more complete set of angle-resolved NEXAFS spectra of $V_2O_5(0\,1\,0)$ become available. In addition, a full comparison requires the extension of the present theoretical treatment to include V 2p to 3d excitations which are found in the experiment. Experimental and theoretical studies along these lines are currently under way.

Acknowledgements

This work has been supported by Deutsche Forschungsgemeinschaft through SFB 546 ‘‘Transition Metal Aggregates’’.

References

[1] Y. Iwasawa, Catal. Today 18 (1993) 21.
[2] O.V. Krylov, Kin. Catal. 40 (1999) 682.
[3] P. Laszlo, J. Phys. Org. Chem. 11 (1998) 356.
[4] G.A. Somorjai, J. Phys. Chem. B 104 (2000) 2969.
[5] G.C. Bond, S.F. Tahir, Appl. Catal. 71 (1991) 1.
[6] H.K. Kung (Ed.), Transition Metal Oxides: Surface Chemistry and Catalysis, in: B. Delmon, J.T. Yates (Eds.), Studies in Surface Sciences and Catalysis, vol. 45, Elsevier, Amsterdam, 1989.
[7] B. Grzybowska-Swierkosz, F. Trifiro, J.C. Vedrine (Eds.), Vanadia Catalysts for Selective Oxidation of Hydrocarbons and Their Derivatives, J. Appl. Catal. 157 (1997) 1.

[8] G. Busca, L. Lietti, G. Ramis, F. Berti, Appl. Catal. B—Environmental 18 (1998) 1.
[9] J.H. Choi, S.K. Kim, Y.C. Bak, Korean J. Chem. Eng. 18 (2001) 719.
[10] E.A. Mamedov, V.C. Corberan, Appl. Catal. A—General 127 (1995) 1.
[11] A. Anillo, M.L. Rodriguez, R. Llavona, J. Rodriguez, M.V. Martinez-Huerta, M.A. Banares, J.L.G. Fierro, Int. J. Inorg. Mat. 2 (2000) 177.
[12] B. Tepper, B. Richter, A.C. Dupuis, H. Kuhlenbeck, C. Hucho, P. Schilbe, M.A. bin Yarmo, H.J. Freund, Surf. Sci. 496 (2002) 64.
[13] V.A. Ranea, J.L. Vicente, E.E. Mola, P. Arnal, H. Thomas, L. Gambaro, Surf. Sci. 463 (2000) 115.
[14] C. Kolczewski, K. Hermann, J. Chem. Phys. 118 (2003) 7599.
[15] Z.M. Zhang, V.E. Henrich, Surf. Sci. 321 (1994) 133.
[16] T. Ohta, J. Electr. Spectr. Rel. Phen. 92 (1998) 131.
[17] J. Taborski, P. Vaterlein, H. Dietz, U. Zimmermann, E. Umbach, J. Electr. Spectr. Rel. Phen. 75 (1995) 129.
[18] P. Srivastava, K. Baberschke, Topics Catal. 10 (2000) 199.
[19] L. Patthey, H. Rensmo, P. Persson, K. Westermark, L. Vayssieres, A. Stashans, A. Petersson, P.A. Bruhwiler, H. Siegbahn, S. Lunell, N. Martensson, J. Chem. Phys. 110 (1999) 5913.
[20] J.G. Chen, Surf. Sci. Rep. 30 (1997) 5.
[21] L.G.M. Pettersson, H. Ågren, Y. Luo, L. Triguero, Surf. Sci. 408 (1998) 1.
[22] M. Nyberg, J. Hasselstrom, O. Karis, N. Wassdahl, M. Weinelt, A. Nilsson, L.G.M. Pettersson, J. Chem. Phys. 112 (2000) 5420.
[23] M. Neuber, M. Zharnikov, J. Walz, M. Grunze, Surf. Rev. Lett. 6 (1999) 53.
[24] V. Carravetta, G. Contini, O. Plashkevych, H. Ågren, G. Polzonetti, J. Phys. Chem. A 103 (1999) 4641.
[25] O. Sipr, A. Simunek, S. Bocharov, Th. Kirchner, G. Dräger, Phys. Rev. B 60 (1999) 14115.
[26] H. Kuhlenbeck, private communication.
[27] K. Hermann, M. Witko, in: D.P. Woodruff (Ed.), The Chemical Physics of Solids Surfaces, Oxide Surfaces, vol. 9, Elsevier Science, Amsterdam, 2001, p. 136.
[28] A. Chakrabarti, K. Hermann, R. Druzinic, M. Witko, F. Wagner, M. Petersen, Phys. Rev. B 59 (1999) 10583.
[29] B. Hammer, L.B. Hansen, J.K. Norskov, Phys. Rev. B 59 (1999) 7413.
[30] J.P. Perdew, K. Burke, M. Ernzerhof, Phys. Rev. Lett. 77 (1996) 3865.
[31] The program package StoBe is a greatly modified version of the DFT-LCGTO program package DeMon, originally developed by A. St.-Amant and D. Salahub (University of Montreal), with extensions by L.G.M. Pettersson and K. Hermann.
[32] J.C. Slater, in: P.O. Loewdin (Ed.), Advances in Quantum Chemistry, Academic, New York, 1972, p. 1.
[33] J.C. Slater, K.H. Johnson, Phys. Rev. B 5 (1972) 844.
[34] H. Ågren, V. Carravetta, O. Vahtras, L.G.M. Pettersson, Theor. Chem. Accounts 97 (1997) 14.
[35] L. Triguero, L.G.M. Pettersson, H. Ågren, Phys. Rev. B 58 (1998) 8097.
[36] N. Godbout, D.R. Salahub, J. Andzelm, E. Wimmer, Can. J. Chem. 70 (1992) 560.
[37] W. Kutzelnigg, U. Fleischer, M. Schindler, in: NMR-Basic Priniciples and Progress, vol. 23, Springer Verlag, Heidelberg, 1990, p. 165.
[38] L.G.M. Pettersson, private communication.
[39] L.G.M. Pettersson, U. Wahlgren, O. Gropen, Chem. Phys. 80 (1983) 7.
[40] C. Kolczewski, R. Püttner, O. Plashkevych, H. Ågren, V. Staemmler, M. Martins, G. Snell, A.S. Schlachter, M. Sant'Anna, G. Kaindl, L.G.M. Pettersson, J. Chem. Phys. 115 (2001) 6426.
[41] E. Goering, O. Müller, M. Klemm, M.L. den Boer, S. Horn, Phil. Mag. B 75 (1997) 229.